

Optical Engineering

OpticalEngineering.SPIEDigitalLibrary.org

Performance of high-voltage CMOS single-photon avalanche diodes with and without well-modulation technique

Michael Hofbauer
Bernhard Steindl
Kerstin Schneider-Hornstein
Horst Zimmermann

SPIE.

Michael Hofbauer, Bernhard Steindl, Kerstin Schneider-Hornstein, Horst Zimmermann, "Performance of high-voltage CMOS single-photon avalanche diodes with and without well-modulation technique," *Opt. Eng.* **59**(4), 040502 (2020), doi: 10.1117/1.OE.59.4.040502

Performance of high-voltage CMOS single-photon avalanche diodes with and without well-modulation technique

Michael Hofbauer,* Bernhard Steindl, Kerstin Schneider-Hornstein, and Horst Zimmermann

TU Wien, Institute of Electrodynamics, Microwave and Circuit Engineering, Vienna, Austria

Abstract. We investigate single-photon avalanche diodes with a thick absorption zone leading to a high photon detection probability in the near-infrared spectrum, e.g., to 27.9% at 850 nm. Furthermore, modulation doping for tuning the breakdown voltage in single-photon avalanche diodes is used. Modulation doping allows for reduction of the effective doping in the structure during the design phase without process modifications. We compare a modulation doped version with a single-photon avalanche diode not using this technique. We prove that both versions are operational. The modulation doped version shows a reduced dark count rate and afterpulsing probability at the cost of a reduced photon detection probability. © 2020 Society of Photo-Optical Instrumentation Engineers (SPIE) [DOI: [10.1117/1.OE.59.4.040502](https://doi.org/10.1117/1.OE.59.4.040502)]

Keywords: single-photon avalanche diode; optoelectronic integrated circuits; modulation doping; photodetectors; adjustable breakdown voltage.

Paper 20200167L received Feb. 13, 2020; accepted for publication Apr. 14, 2020; published online Apr. 29, 2020.

1 Introduction

Single-photon avalanche diodes (SPADs) are utilized in countless applications. They are used, e.g., in mobile phones as a proximity sensor to detect if a face is in front of the phone,¹ in three-dimensional time-of-flight cameras,² and in positron emission tomography scanners as they slowly replace photomultiplier tubes.³ Besides those prominent applications, SPADs are being utilized in many other applications, such as fluorescence microscopy⁴ and quantum cryptography.^{5,6}

SPADs are avalanche photodiodes (APDs) operated above their breakdown voltage. An absorbed photon therefore might trigger a self-sustaining avalanche that can be easily detected and hence allows for detecting a single photon. Before another photon can be detected, the avalanche needs to be stopped; this process is called quenching. This can be achieved by an active quenching circuit, which actively reduces the voltage across the SPAD below its breakdown voltage as soon as an avalanche is detected. Another approach is passive quenching in which the voltage drop across a series resistor during the avalanche is utilized for quenching.

There are several key parameters describing the performance of SPADs.⁷ The most relevant are as follows:

- The photon detection probability (PDP), which is the ratio between detected photons and total incident photons striking the photoactive area.
- The dark count rate (DCR), which describes the count rate that is measured at the output of the detector under dark conditions. These counts are triggered by thermally generated electron–hole pairs or by tunneling events.
- The afterpulsing probability, which gives the probability that after a detection, a second pulse is visible at the output caused by the release of trapped charges shortly after the avalanche or by optical self-crosstalk.⁸

*Address all correspondence to Michael Hofbauer, E-mail: michael.hofbauer@tuwien.ac.at

Another important design parameter of the SPAD is its breakdown voltage. If the breakdown voltage is too low, the depleted layer typically is thin, which reduces the PDP for longer wavelengths, and the electric field strength in the depleted space-charge region is low. If the electric field in the absorption zone is weak, the drift time of photogenerated electrons to the multiplication zone is large, which leads to bit errors of a logical zero after a logical one in an SPAD receiver using nonreturn-to-zero mode.⁹ A larger electric field can reduce such bit errors by reducing the drift time. If the breakdown voltage is too high, some of the maximum ratings of the used technology might be violated. This problem, however, arises only for SPAD breakdown voltages exceeding 100 V in the HV CMOS process used.

Because the doping profiles in commercial processes typically are fixed, it is not trivial to modify the breakdown voltage for a given process flow. In this paper, we present an SPAD with a modulation doped deep p-well and compare it with an SPAD using a standard deep p-well. Modulation doping reduces the effective well doping and hence allows for increasing the breakdown voltage. The modulation degree can be chosen as a design parameter in a certain range, which gives the opportunity to adjust the breakdown voltage. In the linear mode, an accurate comparison of both samples was done in Ref. 10. Using two different quenching circuits, the basic structure without modulation doping was used as SPAD in Refs. 11 and 12.

In the next section, the device structure of the investigated SPADs will be discussed. After that, the key characteristics of both SPADs are compared. In the final section, we conclude.

2 Device Structure

The basic structure of the first SPAD (SPAD1) as shown in the top part of Fig. 1 was described in Ref. 13 as a linear-mode APD and was realized in the same silicon 0.35- μm high-voltage CMOS process. Standard silicon devices can detect light up to a wavelength of ~ 1100 nm.¹⁴ It uses a p-doped wafer with a p-doped epitaxial layer (p-epi) with a thickness of ~ 10 μm . The p-epi layer with a doping concentration of $\sim 1 \times 10^{15}$ cm^{-3} serves as the absorption zone. The multiplication zone is formed at the interface of the highly doped n⁺-cathode and the deep p-well. To eliminate edge breakdown effects, the diameter of the deep p-well is smaller than the cathode diameter. In addition, the deep p-well is embedded in a deep n-well. The deep n-well additionally reduces the effective doping concentration in the deep p-well and thereby increases the resulting breakdown voltage. This enables the epitaxial layer to be depleted prior to breakdown of the SPAD. The used process allows for defining an opto-window above the photosensitive area. In this region, the oxide stack is removed and an antireflection coating is deposited. This reduces interference

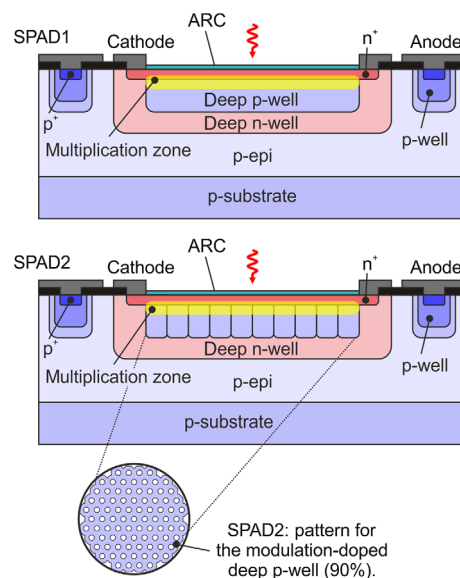


Fig. 1 Cross-section of the SPAD1 and SPAD2 (not to scale).

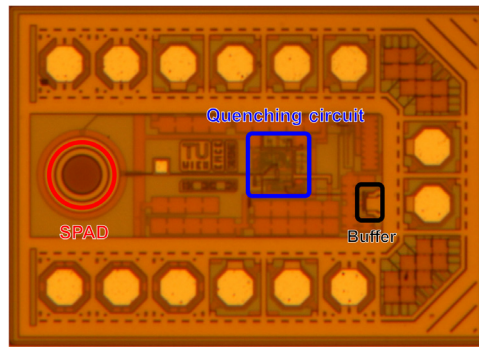


Fig. 2 Microphotograph of the OEIC (SPAD1).

effects and results in a smoother spectral responsivity compared with the case if the light has to pass the oxide stack. The second SPAD (SPAD2), depicted in the bottom part of Fig. 1, has almost the same structure as SPAD1. The only difference is that SPAD2 has a modulation-doped deep p-well, which reduces the effective doping of this well and therefore further increases the breakdown voltage.¹⁵ The aim was to reach a modulation doping factor of $\sim 90\%$. This was accomplished using a specific fill pattern for the deep p-well (i.e., for SPAD1). Holes were created inside the layout mask of this well as depicted in the bottom part of Fig. 1 to prevent the implantation within these holes. The diameter of each hole is $0.9 \mu\text{m}$, and the center-center distance between two holes is $3 \mu\text{m}$. An important factor is that modulation doping does not require any process modifications. It can be implemented during the design phase, which allows for tuning the degree of the modulation doping in a certain range. However, to work properly, the dimensions of the holes and the gaps between the holes need to stay below a technology-dependent limit, which depends on the thermal budget of the process. The active diameter of both devices is $85 \mu\text{m}$ (i.e., the diameter of the deep p-well).

Each SPAD structure is connected to a mixed active-passive quenching circuit. The circuit concept resembles the circuit published in Ref. 16 realized in $0.35\text{-}\mu\text{m}$ standard (digital) CMOS. It consists of a cascoded switching circuit to double the quenching voltage (6.6 V) at a short response time, combined with a fast active quench time to minimize the total charge generated within the avalanche breakdown, which is crucial for minimizing afterpulsing effects. The dead time of the quenching circuit used for the SPADs presented here is tuneable between 5.8 and 33.4 ns . The total dimensions of the realized optoelectronic integrated circuit (OEIC) are $680 \times 980 \mu\text{m}^2$. The microphotograph of the chip with SPAD1 is shown in Fig. 2.

Important parameters of the SPAD such as the breakdown voltage, the DCR, and the afterpulsing probability fluctuate depending on the device position on the wafer. Therefore, we picked three pairs of samples for SPAD1 and SPAD2 at the borders (left, top, and right) and three pairs of samples from the center of a wafer.

3 Results and Discussion

All devices were mounted in a light-tight box on a thermoelectric cooler regulated at room temperature (25°C). The output of the quenching circuit was connected to a NI-5162 digitizer. The recording time for each bias point was 10 s . The DCR and the APP as well as the PDP in this section were measured depending on the excess bias voltage (V_{ex}). The APP is plotted for two different dead times of $t_d = 5.8 \text{ ns}$ and $t_d = 33.4 \text{ ns}$ and the DCR only for $t_d = 33.4 \text{ ns}$.

The DCR and APP results of SPAD1 are shown in Figs. 3(a) and 3(c). The breakdown voltage V_{BD} of this device varies from 65.5 to 70.2 V for the selected samples. Considering only the SPADs from the center of the wafer (SPAD1-center.1-3, dotted lines), the deviation in breakdown voltage is about 0.4 V . The best DCR results were achieved by the samples from the center. However, one DCR curve of the center SPADs is in the same range as the samples from the wafer borders. The ratio at $V_{ex} = 6.6 \text{ V}$ between the highest (140.4 kcps) and lowest (28.8 kcps) DCR is about 4.9 . In addition, the APP [Fig. 3(c)] shows a large spread between the samples.

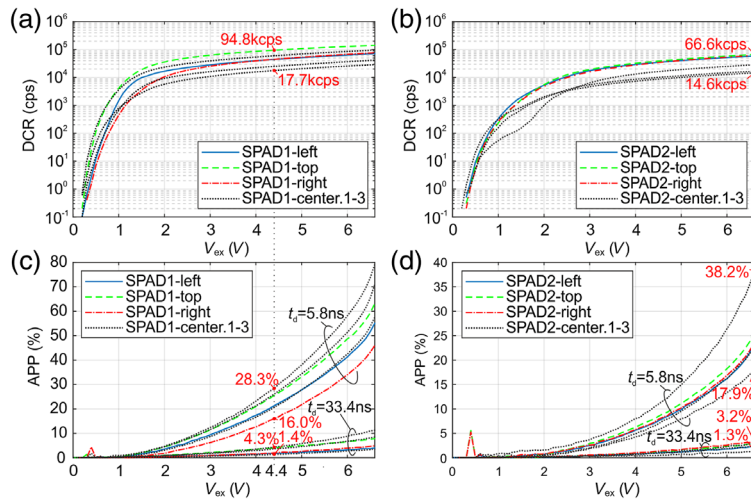


Fig. 3 DCR versus V_{ex} for $t_d = 33.4$ ns: (a) SPAD1, (b) SPAD2; APP versus V_{ex} for $t_d = 5.8$ ns and $t_d = 33.4$ ns: (c) SPAD1, (d) SPAD2.

It varies by a factor of 1.7 and 3.2 at a dead time of $t_d = 5.8$ ns and $t_d = 33.4$ ns, respectively. In contrast to the DCR, samples from the border of the wafer tend to achieve better APP results.

The results of SPAD2 are shown in Figs. 3(b) and 3(d). As mentioned in the previous section, SPAD2 uses a modulation doped deep p-well. This modulation technique forms a well with a reduced effective doping concentration and therefore increases the breakdown voltage. For all samples presented here, V_{BD} varies between 80.1 and 85.5 V. The V_{BD} spread of the center-SPADs is about 0.6 V. It can be clearly seen that the DCR is improved by a factor of ~ 2 compared with SPAD1 for comparable excess bias voltage. Also, the APP is lower for SPAD2 as shown in Fig. 3(b). An explanation for the reduced DCR and APP might be the lower effective excess bias voltage V_{ex} (i.e., the excess bias in relation to the breakdown voltage).^{17,18}

The PDP was corrected for the effects of DCR and APP. Mainly DCR and APP depend on the position on the wafer. Because the used $0.35\text{-}\mu\text{m}$ high-voltage CMOS process is a mature process, a low PDP nonuniformity over the wafer can be expected as in Ref. 19. Therefore, the PDP is plotted only for one sample per structure. The PDP from an SPAD using the same structure as SPAD1 presented in Ref. 12 ($\sim 44\%$ at $V_{ex} = 6.6$ V and $\lambda = 642$ nm) matches almost perfectly with the PDP presented here, as shown in Fig. 4. The PDP indicates the drawback of SPAD2 (Fig. 4). Due to the decreased effective V_{ex} , the PDP is reduced. SPAD1 achieves a maximum PDP of 43.6% in contrast to 30.6% for SPAD2, both at the maximum excess bias voltage of 6.6 V. Thus, a direct comparison of both SPADs should be done for the same PDP. SPAD1 shows a PDP of 30.6% at a V_{ex} of ~ 4.4 V. The DCR and APP values for this V_{ex} are highlighted in Figs. 3(a) and 3(c), respectively. The APP and DCR of SPAD2 are still slightly better (APP: SPAD2: 1.3% to 3.2% at $V_{ex} = 6.6$ V compared with SPAD1: 1.4% to 4.3% at $V_{ex} = 4.4$ V; DCR: SPAD2: 14.6 to 66.6 kcps at $V_{ex} = 6.6$ V compared with SPAD1: 17.7 to 94.8 kcps at $V_{ex} = 4.4$ V) for the longer dead time $t_d = 33.4$ ns. Only one center sample

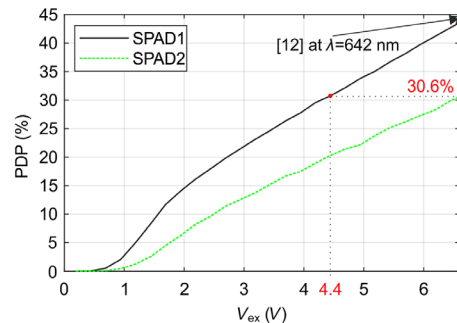


Fig. 4 PDP versus V_{ex} for SPAD1 and SPAD2 at $\lambda = 642$ nm.

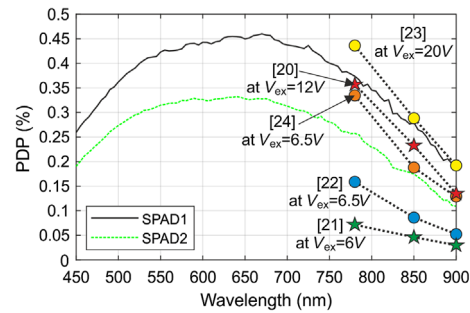


Fig. 5 PDP versus wavelength for SPAD1 and SPAD2 at $V_{ex} = 6.6$ V.

of SPAD2 shows a worse APP (38.2% at $V_{ex} = 6.6$ V compared with 28.3% at $V_{ex} = 4.4$ V for SPAD1) for the shorter dead time $t_d = 5.8$ ns.

As previously shown, the used modulation doping technique increases the breakdown voltage and therefore the electric field strength in the absorption zone. Furthermore, the depleted area additionally expands deeper toward the substrate. Therefore, the spectral distribution of the PDP is shown in Fig. 5 at $V_{ex} = 6.6$ V for SPAD1 and SPAD2. At 780, 850, and 900 nm SPAD1 reaches a PDP of 37.4%, 27.9%, and 18.6%, respectively. For SPAD2, it is 25.7%, 17.5%, and 10.9%, respectively. The maximum PDP of 46.0% of SPAD1 is achieved at a wavelength of $\lambda = 670$ nm. For SPAD2, the maximum PDP of 33.2% is reached at 640 nm. Especially for near-infrared wavelengths, both structures achieve outstanding results compared with integrated CMOS SPADs^{20,21} and comparable results to dedicated SPADs produced in custom processes.^{22–24} The PDPs at wavelengths of 780, 850, and 900 nm of the integrated CMOS SPADs of Refs. 20 and 21 are indicated as stars in Fig. 5, while the PDPs of the SPADs of Refs. 22–24, which use custom processes, are indicated as circles. Please note that for the SPADs of Refs. 20 and 23 considerably larger excess bias voltages were used compared with the other SPADs. The PDP of SPAD1 and SPAD2 could be further improved by increasing the excess bias voltage. The PDPs for the wavelengths of 780, 850, and 900 nm, as well as the used excess bias voltage of SPAD 1 and SPAD 2, are compared with Refs. 20–24 in Table 1.

The noise-equivalent power (NEP) is frequently used to compare the performance of different detectors. For SPADs the NEP is defined as

$$\text{NEP} = \frac{hc}{\lambda} \sqrt{\frac{2\text{DCR}}{\text{PDP}}}, \quad (1)$$

where h is the Planck constant, c is the speed of light in vacuum, and λ is the wavelength of the used light.²⁵ The smaller the value is, the better the performance of the detector is. In Table 2, the NEPs of SPAD1 and SPAD2 are compared for the wavelengths of 780, 850, and 900 nm. For both detectors, the one with the smallest DCR has been selected. SPAD1 has a slightly better

Table 1 Comparison with the state-of-the-art.

SPAD	V_{ex} (V)	Technology	PDP @ 780 nm (%)	PDP @ 850 nm (%)	PDP @ 900 nm (%)
SPAD1	6.6	0.35- μm HV-CMOS	37.4	27.9	18.6
SPAD2	6.6	0.35- μm HV-CMOS	25.7	17.5	10.9
Ref. 20	12	130 nm CMOS	35.8	23.4	13.6
Ref. 21	6	0.35- μm CMOS	7.3	4.8	2.7
Ref. 22	6.5	Custom	15.9	8.6	5.2
Ref. 23	20	Custom	43.6	28.8	19.2
Ref. 24	6.5	Custom	33.5	18.8	12.9

Table 2 NEP of SPAD1 and SPAD2 at $V_{ex} = 6.6$ V.

SPAD	V_{ex} (V)	NEP @ 780 nm (aW/ $\sqrt{\text{Hz}}$)	NEP @ 850 nm (aW/ $\sqrt{\text{Hz}}$)	NEP @ 900 nm (aW/ $\sqrt{\text{Hz}}$)
SPAD1	6.6	78.3	90.7	111.1
SPAD2	6.6	85.8	104.0	131.8

NEP than SPAD2. Nevertheless, the difference is only minor and the NEP can easily be tuned by changing the active area or the temperature of the detector as this mainly influences the DCR, while the PDP is barely affected.

4 Conclusion

In this paper, we compare two SPAD structures realized in a 0.35- μm high-voltage CMOS process. The only difference between these two structures is the used deep p-well forming the multiplication layer. The first SPAD uses the standard deep p-well of the HV CMOS process and achieves outstanding PDP values of 27.9% at 850 nm and 18.6% at 900 nm. For SPAD2, modulation doping was used to reduce the effective doping concentration to increase the breakdown voltage. This strengthens the electric field inside the absorption zone and results in a thicker depleted space-charge region. In linear mode when the device is used as an APD, this results in an increased bandwidth of the structure. In this paper, we prove that modulation doping is an effective way to change the breakdown voltage of a given SPAD structure. The presented SPAD using modulation doping shows reduced DCR and APP compared with the version without modulation doping. The DCR and APP (for the longer dead time of 33.4 ns) of the modulation doped SPAD are on average about 27% and 20% lower than that of SPAD1 for the same PDP (30.6%) at 642 nm. However, the increased breakdown voltage results in a lower effective excess bias voltage and therefore in a reduced PDP. Nevertheless, the presented PDP results of the modulation-doped SPAD for near-infrared light of 17.5% at 850 nm and 10.9% at 900 nm are still comparable to state-of-the-art SPADs (CMOS integrated and custom processes).

Acknowledgments

The authors acknowledge financial support from the Austrian Science Fund (FWF) under Grant No. P28335-N30.

References

1. L. Stark, J. M. Raynor, and R. K. Henderson, "Object detection system using SPAD proximity detectors," *Proc. SPIE* **8167**, 81672A (2011).
2. D. Stoppa et al., "A CMOS 3-D imager based on single photon avalanche diodes," *IEEE Trans. Circuits Syst. I* **54**(1), 4–12 (2007).
3. V. C. Spanoudaki and C. S. Levin, "Photo-detectors for time of flight positron emission tomography (ToF-PET)," *Sensors* **10**(11), 10484–10505 (2010).
4. X. Michalet et al., "Silicon photon-counting avalanche diodes for single-molecule fluorescence spectroscopy," *IEEE J. Sel. Top. Quantum Electron.* **20** (6), 248–267 (2014).
5. R. H. Hadfield, "Single-photon detectors for optical quantum information applications," *Nat. Photonics* **3**(12), 696–705 (2009).
6. K. J. Gordon et al., "A short wavelength gigahertz clocked fiber-optic quantum key distribution system," *IEEE J. Quantum Electron.* **40**, 900–908 (2004).
7. M. Fishburn, "Fundamentals of CMOS single-photon avalanche diodes," PhD Thesis, Delft University of Technology, The Netherlands (2012).
8. H. Mahmoudi et al., "Statistical study of intrinsic parasitics in an SPAD-based integrated fiber optical receiver," *IEEE Trans. Electron. Dev.* **66**(1), 497–504 (2019).

9. H. Zimmermann et al., “Integrated fiber optical receiver reducing the gap to the quantum limit,” *Sci. Rep.* **7**, 2652 (2017).
10. R. Enne, B. Steindl, and H. Zimmermann, “Speed optimized linear-mode high-voltage CMOS avalanche photodiodes with high responsivity,” *Opt. Lett.* **40**(19), 4400–4403 (2015).
11. B. Steindl, R. Enne, and H. Zimmermann, “Thick detection zone single-photon avalanche diode fabricated in 0.35 μm complementary metal-oxide semiconductors,” *Opt. Eng.* **54**(5), 050503 (2015).
12. A. Dervić et al., “High-voltage active quenching and resetting circuit for SPADs in 0.35 μm CMOS for raising the photon detection probability,” *Opt. Eng.* **58**(4), 040501 (2019).
13. B. Steindl et al., “Linear mode APD with high responsivity integrated in high-voltage CMOS,” *IEEE Electron. Dev. Lett.* **35**(9), 897–899 (2014).
14. H. Zimmermann, *Silicon Optoelectronic Integrated Circuits*, Springer Nature, Switzerland (2018).
15. R. Enne, B. Steindl, and H. Zimmermann, “Improvement of CMOS-integrated vertical APDs by applying lateral well modulation,” *IEEE Photonics Technol. Lett.* **27**(18), 1907–1910 (2015).
16. R. Enne et al., “Fast cascoded quenching circuit for decreasing after pulsing effects in 0.35- μm CMOS,” *IEEE Solid-State Circuits Lett.* **1**(3), 62–65 (2018).
17. H. Dautet et al., “Photon counting techniques with silicon avalanche photodiodes,” *Appl. Opt.* **32**, 3894–3900 (1993).
18. S. Cova et al., “Avalanche photodiodes and quenching circuits for single-photon detection,” *Appl. Opt.* **35**, 1956–1976 (1996).
19. S. Burri, C. Bruschini, and E. Charbon, “LinoSPAD: a compact linear SPAD camera system with 64 FPGA-based TDC modules for versatile 50 ps resolution time-resolved imaging,” *Instruments* **1**(1), 6 (2017).
20. E. A. G. Webster, L. A. Grant, and R. K. Henderson, “A high-performance single-photon avalanche diode in 130-nm CMOS imaging technology,” *IEEE Electron. Dev. Lett.* **33**(11), 1589–1591 (2012).
21. D. Bronzi et al., “Low-noise and large-area CMOS SPADs with timing response free from slow tails,” in *Proc. Eur. Solid-State Device Res. Conf. (ESSDERC)*, Bordeaux, pp. 230–233 (2012).
22. F. Ceccarelli et al., “152-dB dynamic range with a large-area custom technology single-photon avalanche diode,” *IEEE Photonics Technol. Lett.* **30**(4), 391–394 (2018).
23. A. Gulinatti et al., “New silicon SPAD technology for enhanced red-sensitivity, high-resolution timing and system integration,” *J. Mod. Opt.* **59**(17), 1489–1499 (2012).
24. F. Acerbi et al., “High detection efficiency and time resolution integrated-passive-quenched single-photon avalanche diodes,” *IEEE J. Sel. Top. Quantum Electron.* **20**(6), 268–275 (2014).
25. D. Bronzi et al., “SPAD figures of merit for photon-counting, photon-timing, and imaging applications: a review,” *IEEE Sens. J.* **16**(1), 3–12 (2016).

Michael Hofbauer received his Dipl.-Ing. degree in electrical engineering from TU Wien (Vienna University of Technology) in 2011 and became university assistant in 2016. In 2017 he received his doctor degree from TU Wien. He finished his doctoral studies sub auspiciis Praesidentis (i. e. with highest possible honors). His main fields of research are opto-electronic integrated circuits, single-photon detectors, integrated photonics, distance measurements, and single-event effects. He authored and coauthored more than 60 publications.

Bernhard Steindl received his Dipl.-Ing. and the Dr. techn. degree in electrical engineering from TU Wien (Vienna University of Technology), Vienna, Austria, in 20013 and 2020, respectively. Since 2011 he has been with TU Wien, Institute of Electrodynamics, Microwave and Circuit Engineering. His fields of interests are integrated analog circuit design, simulation, design and characterisation of integrated photoreceivers and optoelectronics in general.

Kerstin Schneider-Hornstein received her Dipl. Ing. degree in 2000 and the Dr. techn. degree in 2004 from the TU Wien (TUW), Vienna, Austria. Since 2001 she is with TUW, Institute of

Electrodynamics, Microwave and Circuit Engineering. Her major fields of interest are optoelectronics, photonic-electronic integration, and integrated circuit design. She is author of the Springer book “Highly Sensitive Optical Receivers” and author and co-author of more than 55 journal and conference papers.

Horst Zimmermann became Dr.-Ing. in 1991 and was then Alexander-von-Humboldt Research-Fellow at Duke University working on diffusion in Si, GaAs, and InP. In 1993, he joined Kiel University working on optoelectronic integration. Since 2000 he is full professor for circuit engineering at TU Wien working on (Bi)CMOS analog and optoelectronic fullcustom integrated circuits. He is author of two Springer books and coauthor of more than 550 publications. In 2002 he became a Senior Member of IEEE.